Published in final edited form as:
Magn Reson Med. 2012 October ; 68(4): 1074–1086. doi:10.1002/mrm.23312.

CEST phase mapping using a Length and Offset VARied Saturation (LOVARS) scheme

Xiaolei Song[1,2], **Assaf A. Gilad**[1,2,5], **Suresh Joel**[2,5], **Guanshu Liu**[2,5], **Amnon Bar-Shir**[1,2], **Yajie Liang**[1,2], **Michael Gorelik**[1,2], **James J. Pekar**[2,5], **Peter C.M. van Zijl**[2,5], **Jeff W.M. Bulte**[1,2,3,4,5], and **Michael T. McMahon**[2,5,*]

[1]Cellular Imaging Section and Vascular Biology Program, Institute for Cell Engineering, The Johns Hopkins University School of Medicine, Baltimore, Maryland [2]Russell H. Morgan Department of Radiology and Radiological Science, Division of MR Research, The Johns Hopkins University School of Medicine, Baltimore, Maryland [3]Department of Biomedical Engineering, The Johns Hopkins University School of Medicine, Baltimore, Maryland [4]Department of Chemical & Biomolecular Engineering, The Johns Hopkins University School of Medicine, Baltimore, Maryland [5]F.M. Kirby Research Center for Functional Brain Imaging, Kennedy Krieger Institute, Baltimore, Maryland

Abstract

Chemical exchange saturation transfer (CEST) MRI is a promising new technique for cellular and molecular imaging. This contrast allows the detection of tumors and ischemia without the use of gadolinium as well as the design of microenvironment-sensitive probes that can be discriminated based on their exchange contrast properties and saturation frequency. Current acquisition schemes to detect and analyze this contrast suffer from sensitivity to spatial B_0 inhomogeneity and low contrast-to-noise-ratio (CNR), which is an obstacle to widespread adoption of the technology. A new method to detect CEST contrast is proposed here, termed “Length and Offset VARied Saturation” or “LOVARS”, which acquires a set of images with the saturation parameters varied so as to modulate the exchange contrast. Either fast fourier transform or the general linear model can be employed to decompose the modulation patterns into separate sources of water signal loss. After transformation, a LOVARS phase map is generated, which is insensitive to B_0 inhomogeneity. When collected on live mice bearing 9L gliosarcomas, and compared to the conventional MTR_{asym} map using offset increment correction, the results show that LOVARS phase mapping obtains about four times higher CNR and exhibits less B_0 artifacts.

INTRODUCTION

Since the first report of Chemical Exchange Saturation Transfer (CEST) contrast in 2000(1), this imaging technology has attracted many new research studies (2–5), resulting in a number of pre-clinical (6–13) and now also clinical applications (13,14). Endogenous CEST contrast has been applied to charaterizing acute ischemia (7,15) and brain tumors (8,14,16), visualizing the concentration of tissue amide protons and their chemical exchange rate. CEST contrast has been found to relate to tumor grade (14), and allows separation of recurrent tumor from the effects of treatment (8). This contrast is also used in musculoskeletal imaging for monitoring glycosaminoglycan concentrations in cartilage (13). In addition, CEST reporter genes are being developed allowing detection of cells expressing this gene (6). An important advantage of CEST is the capability to design agents with

*To whom correspondence should be addressed. Telephone (410) 502-8188, Fax: (410) 614-3147, mcmahon@mri.jhu.edu.

protons at different frequencies, allowing simultaneous detection of probes with different functions (17,18). CEST probes have been designed to label virus particles (10,19), allow imaging of the kidneys (9,11), and allow the detection of peptides (17,20), drug delivery particles (4,21–23), changes in temperature (24), pH (9,25,26), and metabolite concentrations (27,28). Ultimately, for both endogenous and exogenous CEST contrast agent studies, improved detection technologies will be important to speed up the transition to widespread pre-clinical and clinical use.

CEST contrast is produced through the application of a radiofrequency (RF) saturation pulse at the resonance frequency of the exchangeable protons, after which the resulting saturation is transferred via chemical exchange to bulk water leading to a loss in signal that yields contrast. However, the application of this pulse results in other sources of water signal loss such as due to conventional magnetization transfer contrast (MTC, mainly from solid-like macromolecules in tissue) (29,30) and direct saturation (DS) (31), complicating image analysis. In order to analyze the sources of water signal loss, it is widespread practice to plot the saturated water signal intensity (S) normalized with the intensity without saturation (S_0) as a function of saturation offset with respect to water, termed a Z-spectrum (32). As shown in Fig.1, the symmetries of the DS and MTC signals with respect to the water frequency (assigned to 0 ppm) differ from CEST. Because CEST contrast is asymmetric with respect to the water frequency, the conventional way to detect and quantify CEST contrast has been by calculating the asymmetry in the magnetization transfer ratio (MTR_{asym}) at the frequency of the exchangeable protons($\Delta\ \omega$) :

$$MTR_{asym}=\frac{(S(-\Delta\omega)-S(+\Delta\omega))}{S_0} \quad [1]$$

The proton transfer ratio (PTR) (33) is a metric used to describe CEST contrast for a certain proton type in a given agent. Unfortunately the standard assumption that the experimentally determined MTR_{asym} equals PTR is not valid as MTC may have an inherent asymmetric component ($MTR_{asym}^{inherent}$) (34,35). Moreover, the spatial inhomogeneity of magnetic field results in water frequency variations and produces artifacts (MTR_{asym}^{field}). Therefore, the experimentally measured asymmetry is given by:

$$MTR_{asym}=PTR+MTR_{asym}^{field}+MTR_{asym}^{inherent} \quad [2]$$

Errors in MTR_{asym} due to MTR_{asym}^{field} contributions can be reduced by mapping the field and performing a voxel-based offset correction, which we categorized as Offset Incrementation Correction (OIC) methods. Mapping the field can be accomplished through fitting the Z-spectrum (36,37) for each pixel or through gradient echo based methods or fitting Z-spectra acquired using short, weak saturation pulses (38–40). The corrected contrast map is generated by acquiring a reduced number of images with frequencies around the proton of interest. Such types of either partial or whole Z-spectra acquisition require relatively long scan times and have the disadvantage that the CNR of the contrast map doesn't increase as the number of offsets and the scan time increase. To partially compensate for this, CEST contrast can also be calculated by integrating over the width of the CEST peak (41,42) or using a Lorentzian line-fitting (43), but still require sweeping the offset over a wide range. Recently an additional method has been proposed (44) which utilizes two saturation frequency alternating to cancel out the MTR_{asym}^{field} and $MTR_{asym}^{inherent}$.

We propose here a different approach, termed Length and Offset VARied Saturation (LOVARS), in which the length (t_{sat}) and offset ($\Delta\omega$) of the saturation pulse is varied to

cosine modulate the water signal loss and impart differential phases on the three different components of the asymmetric MTR contributions (PTR, $MTR_{asym}^{inherent}$, and MTR_{asym}^{field}). This allows their separation using post-processing techniques similar to those for analyzing time-varying signals in fMRI (45–51), such as the general linear model (GLM) to identify modulation patterns or fast fourier transform (FFT) to separate different frequency components. We tested the LOVARS scheme *in vivo* on mice bearing 9L gliosarcomas, which is known to produce a well-characterized endogenous CEST (amide proton transfer, APT) contrast (52).

THEORY

The sources of water signal loss upon application of a saturation pulse (MTC, PTR, DS) can be described using modified Bloch equations (29,33,53–55). The t_{sat}-dependence of CEST contrast (PTR) can be modeled using (33):

$$\mathrm{PTR}(t_{sat})=\frac{k_{sw}\cdot\alpha\cdot X_s}{R_{1w}+k_{sw}\cdot X_s}\times[1-e^{-(R_{1w}+k_{sw}\cdot X_s)t_{sat}}] \quad [3]$$

with k_{sw} the unidirectional exchange rate from solute protons to water protons, X_S the concentration of the solute exchangeable protons, R_{1w} the spin-lattice relaxation rate of water, α the saturation efficiency. This expression has been used to measure k_{sw} for poly-L-lysine (PLL), dendrimers, and other CEST agents *in vitro* (17,56) based on this exponential buildup as a function of t_{sat} (56).

Saturation pulses also produce a direct loss in water magnetization due to saturation of water protons. The longitudinal magnetization after applying an RF pulse in the absence of CEST agent can be modeled (54,57):

$$M_z(t_{sat})=\frac{[(R_2+\alpha_1)^2+\Delta\omega^2](R_1+\alpha_1)}{\alpha_1(\alpha_1-\alpha_2)(\alpha_1-\alpha_3)}e^{\alpha_1\cdot t_{sat}}+\cos(\frac{\sqrt{3}}{2}(A-B))\frac{[(R_2+\alpha_2)^2+\Delta\omega^2](R_1+\alpha_2)}{\alpha_2(\alpha_2-\alpha_1)(\alpha_2-\alpha_3)}e^{[\frac{-(2R_2+R_1)}{3}-\frac{A+B}{2}]t_{sat}}$$

where $\alpha_1=\frac{-(2R_2+R_1)}{3}+A+B$, $\alpha_2=[\frac{-(2R_2+R_1)}{3}-\frac{A+B}{2}]+i\frac{\sqrt{3}}{2}(A-B)$ and, $\alpha_3=\alpha_2^*$ in which $A=[-\frac{b}{2}+\sqrt{c}]^{\frac{1}{3}}$, $B=[-\frac{b}{2}-\sqrt{c}]^{\frac{1}{3}}$, $b=\frac{1}{27}(R_1$

$-R_2)[2(R_1-R_2)^2+18(\Delta\omega)^2-9\omega_1^2]$, $c=\frac{1}{27}\{[(\Delta\omega)^2+\omega_1^2]^3+(R_1-R_2)^2(2(\Delta\omega)^2[2(\Delta\omega)^2+(R_1-R_2)^2]-\omega_1^2[\frac{\omega_1^2}{4}+5($

. Eq.[4] shows that the buildup of DS with t_{sat} is related to the relaxation rates for water (R_1, R_2), Δω, and ω_1. As shown in Eqs.[3,4], the PTR and DS contrast dependencies on t_{sat} are different and we will show later using both simulations and experiments that MTC also possesses a different dependence on t_{sat}.

Design of LOVARS Scheme

Based on the knowledge that CEST, DS and MTC behave differently as a function of t_{sat} and using the symmetry properties of DS and MTC (predominantly symmetric) and CEST (asymmetric) around the water resonance, the LOVARS imaging scheme was designed (Fig. 2). For this scheme, we acquire a series of images using *N* LOVARS' Units (LUs) with four images within each LU (Fig.2a):

$$[S_1,S_2,S_3,S_4]=[S(-\Delta\omega,T_{sat,2}),S(-\Delta\omega,T_{sat,1}),S(+\Delta\omega,T_{sat,2}),S(+\Delta\omega,T_{sat,1})] \quad [5]$$

where $S(-\Delta\omega, T_{sat,2})$ represents the image signal with a saturation pulse with offset $-\Delta\omega$ and length $T_{sat,2}$. Two different offsets are used: 1) $+\Delta\omega$, on resonance with the exchangeable protons and 2) $-\Delta\omega$, on the opposite side of water from the exchangeable protons, and two different t_{sat} values, a longer one ($T_{sat,1}$) and a shorter one ($T_{sat,2}$). Assuming no B_0 inhomogeneity (Fig.1), DS and MTC are mostly symmetric and therefore the signal loss for $+\Delta\omega$ and $-\Delta\omega$ are the same for a given t_{sat} resulting in 2 oscillations/LU as shown in Fig.2b. In contrast, for CEST agents such as PLL, signal loss occurs when the saturation pulse is on resonance with the protons ($+\Delta\omega$) and not when the pulse is on the opposite side of water ($-\Delta\omega$), leading to only 1 oscillation/LU (Fig.2b).

Considering the combined contributions of CEST, DS, and MTC, the pattern of water signal can be represented by the LOVARS Response Function (LRF):

$$S_{LRF}=A_0+A_1\cdot\cos[\pi/2(m-1)+\varphi]+A_2\cdot\cos[\pi(m-1)] \quad [6]$$

where 'm' is the image number in the LOVARS time series (m=1,2,…,4*X*N) after acquiring N LUs, cos $(\pi/2(m-1)+\varphi)$ represents the asymmetric components of the contrast (Eq.[1]) and cos$(\pi\ (m-1))$ represents the symmetric components of the contrast (Fig.1c) with respect to frequency offset. In addition, A_0 represents the mean water signal (DC bias), A_1, A_2 are amplitudes of the two cosine functions with different frequencies, and φ is the phase of the cosine modulation at the frequency of 1 cycle/LU. These parameters can be determined using either GLM or FFT. Figs.2b&c show the LOVARS signal pattern for PLL and L-arginine respectively, with both fit to Eq.[6]. The pattern for PLL is predominantly due to CEST contrast. For L-arginine the pattern contains both CEST and DS effects due to the closeness of the exchangeable protons chemical shift to water (1.8 ppm).

LOVARS Post-Processing

The LOVARS scheme creates modulations in the water signal that can be analyzed in multiple ways. One possibility is to FFT the signal intensity in the LOVARS time series to determine the contributions of CEST contrast (Fig.2c). According to the Discrete Fourier Transform of the acquisition pattern in Eq.[5] (normalized by S_0), for the nth LU (n=1,2, …,N), the transformed signal in LOVARS frequency domain is:

$$L(k)=\frac{1}{S_0}\sum_{l=1}^{4}S_{l,n}\cdot e^{(-\frac{2\pi i}{4})\cdot(l-1)k} \quad [7]$$

where k is in units of cycles/LU and l is the image index within one LU. For k = 1 cycle/LU, expanding Eq.[7] using $e^{(-\frac{2\pi i}{4})\cdot(l-1)}=\cos(-\frac{2\pi i}{4})\cdot(l-1)+i\cdot\sin(-\frac{2\pi i}{4})\cdot(l-1)$ gives:

$$L(1\ \text{cycle/LU}) =\frac{1}{S_0}[(S_{1,n}-S_{3,n})-i(S_{2,n}-S_{4,n})]=\frac{1}{S_0}[S(-\Delta\omega,T_{sat,2})-S(+\Delta\omega,T_{sat,2})]-i[S(-\Delta\omega,T_{sat,1})-S(+\Delta\omega,T_{sat,1})]=MTR_{asym} \quad [8]$$

L(1 cycle/LU) relates in a straightforward manner to MTR_{asym}. The imaginary part of L(1 cycle/LU) corresponds to the MTR_{asym} produced using the longer saturation pulse, MTR_{asym} ($T_{sat,1}$), while the real part corresponds to the MTR_{asym} using a shorter saturation pulse, MTR_{asym} ($T_{sat,2}$). The relative phase between these two amplitudes (φ) is determined by $\tan(\varphi) = MTR_{asym}(T_{sat,1})/MTR_{asym}(T_{sat,2})$. When the two saturation lengths are chosen such that for CEST contrast: $PTR(T_{sat,1}) > PTR(T_{sat,2})$, while for MTC or DS: $MTR_{asym}^{field}(T_{sat,1}) \le MTR_{asym}^{field}(T_{sat,2})$, the phase can be considered a new CEST contrast parameter that accounts for differences in the t_{sat}-dependence between PTR, $MTR_{asym}^{inherent}$ and MTR_{asym}^{field} (Eq.[2]). Alternatively, GLM (commonly applied in fMRI) can be used to process the images using Eq.[6] as a model.

MATERIALS AND METHODS

Simulations

To estimate the optimal saturation parameters for LOVARS, we performed simulations on two different CEST contrast agents: PLL and L-arginine, using the numerical solutions for 2-pool and 3-pool models, respectively (55,56). The PLL simulations were performed as described previously (56). The L-arginine simulations were performed using two solute pools 'a', chemical shift difference = 1.1 ppm (amine), and 'b', chemical shift difference = 2 ppm (guanidyl amine) and a water pool 'w'. The Bloch equations were written in the general form $d\boldsymbol{Y}/dt = \boldsymbol{A}*\boldsymbol{Y} + \boldsymbol{b}$ (17,55,56) and solved using MATLAB (The MathWorks, Inc., Natick, MA, USA). Based on fitting the three pools in L-arginine at 11.7T, the relaxation rates are: $R_{1w}=0.3\text{sec}^{-1}$, $R_{1a}=R_{1b}=0.71\text{sec}^{-1}$, $R_{2w}=1\text{sec}^{-1}$, $R_{2a}=32\text{sec}^{-1}$ and $R_{2b}=50\text{sec}^{-1}$, and the exchange rates are $k_{aw}=150\text{sec}^{-1}$, $k_{bw}=800\text{sec}^{-1}$ and $k_{ab}=100\text{sec}^{-1}$ with the saturation $B_1=3.8\mu\text{T}$. For 10mM L-arginine the relative molar concentration of exchangeable protons to water protons ($[H^{exch}]_{solute}/[H]_{H_2O}$) is $0.27*10^{-3}$ for pool 'a' and $0.36*10^{-3}$ for pool 'b'. For the simulations including noise, 1%, 2%, 3% Gaussian white noise with mean of zero was added to the L-arginine simulations using MATLAB function 'randn'.

Additionally simulations were carried out to model the t_{sat} dependence of MTC. We simulated data acquired on agar, a model of tissue magnetization transfer, by numerically solving the Bloch equations using a 2-pool model (29,58). The Z-spectra were first simulated at several different concentrations (2%, 3% and 4%) of agar using the relaxation and exchange rates: $R_{1s} = 1\text{sec}^{-1}$, $R_{2s} = 2.23*10^5\text{sec}^{-1}$, $R_{1w} = 0.35\text{sec}^{-1}$, $R_{2w} = 1.3\text{sec}^{-1}$, and $k_{sw} = 176\text{sec}^{-1}$. To determine the t_{sat} dependence of $MTR_{asym}^{inherent}$ and MTR_{asym}^{field}, we shifted the offset of the saturation pulse and calculated the difference in water signal resulting from the saturation pulse (e.g., if the water frequency is shifted by 0.1 ppm, then the original offsets $+\Delta\omega$ and $-\Delta\omega$ would shift to $+\Delta\omega - 0.1$ppm and $-\Delta\omega - 0.1$ ppm, respectively) as a function of t_{sat}.

Phantom Preparation

We prepared a phantom that includes 4 types of samples: a CEST contrast agent (L-arginine), two MTC molecular models (cross-linked bovine serum albumin(BSA) and agar) and 0.01M phosphate-buffered saline (PBS), pH = 7.4, which should only show direct saturation. All samples were dissolved in PBS and placed into 1mm capillary tubes. L-arginine (Sigma, St Louis, MO) samples were prepared at four concentrations (10mM, 5mM, 2.5mM and 1.25mM) to produce a range of CEST contrast. Crosslinked BSA samples (2.5% and 5%) were prepared using bovine serum albumin(Sigma, St Louis, MO) by heating this for 8min in a water bath at 80°C. Agar samples were prepared at concentrations of 2%, 3% and 4% w/v.

Brain Tumor Studies

Rat gliosarcoma cells (9L) were grown in standard medium, collected by trypsinization, washed, and suspended in medium at a concentration of 1×10^5 cells/μL. Balb/c NOD/SCID male mice (6–8 weeks old; n=7, ~25g weight) were initially anesthetized in a chamber containing 4~5% isoflurane. The animals were positioned in a stereotactic device (Stoelting Lab Standard), a small midline skin incision was made to expose the skull, and a 1mm^2 hole was drilled 2mm to the right of the bregma. Cells (2×10^5/2 μL) were injected into the striatum, 2.5mm ventral to the surface of the brain, slowly over a period of 3min with the syringe removed 30sec after completion to minimize back flow.

For MRI, mice were anesthetized using 0.5–2% isoflurane. Immediately following the last MRI, mice were perfused with PBS followed by 4% paraformaldehyde(PFA), brains were removed, preserved in 4% PFA at 4°C for a week, cryosectioned (25μm thick), and stained using hematoxylin and eosin (H&E).

MRI Acquisition

In vitro (phantoms)—All experiments were performed on an 11.7 T vertical bore Bruker Avance system (Bruker Biospin, Billerica, MA) with a 15mm birdcage RF coil. The imaging sequence consists of a continuous-wave (CW) saturation pulse and a rapid acquisition with relaxation enhancement (RARE) sequence (RARE factor=8). Other imaging parameters were: field of view (FOV) = 1.15×1.15cm, acquisition matrix size = 64×64, slice thickness = 0.5 mm. The scanning protocol is similar to that described previously(40). At the beginning of the session, a group of images were acquired with $\Delta\omega$ incremented from −0.6 ppm to 0.6 ppm (0.1 ppm step), t_{sat} = 500 msec, B_1 = 0.5 μT, and repetition time (TR) / echo time (TE) = 2200 msec / 4.9 msec to generate the B_0 map using water saturation shift referencing (WASSR) (39). Then a second set of saturation images was collected with $\Delta\omega$ from −5 to 5 ppm (0.3 ppm step), t_{sat} = 4.0 sec, B_1 = 3.8 μT, TR/TE = 6000 msec / 4.9 msec, and number of averages (NA) equals 1 to generate the Z-spectrum. Another three pairs of saturation images (NA=2), with saturation offsets of ± 1.55 ppm, ± 1.8 ppm and ± 2.05 ppm for L-arginine are collected for the contrast map using OIC. For optimizing LOVARS, images were first acquired with t_{sat} varied from 0.5 sec to 5 sec. The final LOVARS images used two LUs, $\Delta\omega$ = +1.8 ppm or −1.8 ppm, $T_{sat,2}$ = 1.5 sec, and $T_{sat,1}$ = 4 sec. An image without saturation pulse (S_0) was collected as intensity reference.

In vivo—All experiments were performed on a 9.4 T horizontal bore animal Bruker Avance system with a 25 mm sawtooth coil. After acquiring T_2-weighted scout images, a 1 mm thick coronal slice at the center of the tumor was chosen for collection of both OIC and LOVARS images. The pulse sequences were kept similar to the phantom studies with the following modifications. First, WASSR B_0 map images were collected with $\Delta\omega$ incremented from −0.5 ppm to 0.5 ppm (0.1 ppm step), t_{sat} = 500 msec, B_1 = 0.5 μT, TR/$TE_{effective}$ = 1500 msec / 14.6 msec and NA = 2, which was used for Scheme 2 OIC maps. After this, a Z-spectrum with $\Delta\omega$ incremented from −4 ppm to +4 ppm (0.25 ppm step or use the scheme in Table 2 of (14)) was collected using t_{sat} = 3000 msec, B_1 = 3 μT, TR/TE = 5000ms / 14.6 ms, NA = 1. Another 3 pairs of the saturation images (NA = 2) were collected with offsets at ± 3.25 ppm, ± 3.5 ppm and ± 3.75 ppm respectively to generate the MTR_{asym} map using Scheme 1 for OIC as described previously(14,36). For optimizing LOVARS, images were acquired with t_{sat} varied from 0.8 sec to 4 sec. The final LOVARS images used 2 LUs, $\Delta\omega$ = +3.5 ppm or −3.5 ppm, $T_{sat,2}$ = 0.8 sec, and $T_{sat,1}$ = 3 sec. An image without saturation pulse (S_0) was collected as a reference. The remaining imaging parameters were matrix size = 128 × 64, FOV = 1.65 × 1.5 cm.

For 3 mice, for tumor identification, additional T_1-weighted (T_1-w) Gd-DTPA images were collected after tail vein injection of 0.4 mmol/kg mouse body weight Gd-DTPA (Magnevist®). T_1-w images with the same FOV and resolution were acquired prior to injection and every 30sec until 15 minutes after injection. The imaging parameters were: TR/TE = 1000msec/7msec, RARE factor = 2, and NA = 1.

MRI Post-processing

All processing was performed using custom-written scripts in Matlab as described in the supplemental information.

RESULTS

Simulations and phantom study

All simulations and phantom experiments were performed at 11. 7T.

T_{sat}-Dependence Features—To design the LOVARS scheme (Fig.2), we collected experimental data from a phantom consisting of 1mm capillaries containing L-arginine (CEST agent) or agar (MTC agent). The simulated Z-spectra and MTR_{asym} (for L-arginine) curves were fit to the experimental data (Fig.3a). Additional simulations were performed to model the t_{sat}-dependence of the CEST and MTC agents. The simulations in Fig.3b demonstrate that for L-arginine the difference between the water signals $S(+\Delta\omega)/S_0$ and $S(-\Delta\omega)/S_0$ continue to increase with increasing t_{sat}. In contrast, for agar with a B_0 shift = 0.3 ppm, after t_{sat} exceeds 1.5sec~2sec, the separation between $S(+\Delta\omega-0.3\text{ ppm})/S_0$ and $S(-\Delta\omega-0.3\text{ ppm})/S_0$ no longer increases. If there is no B_0 inhomogeneity, the overall $MTR_{asym} = 0$ for agar, with B_0 inhomogeneity MTR_{asym}^{field} is non-zero (Eq.[2]) leading to the overall $MTR_{asym} \neq 0$. To determine the optimal $T_{sat,1}$ and $T_{sat,2}$ for LOVARS, we plotted the MTR_{asym} as a function of t_{sat}. After 1.5sec, the t_{sat}-dependence curves for agar plateau regardless of the shift in B_0 (Fig.3c). However, as shown for two different concentrations of L-arginine, the MTR_{asym} continues to increase. Therefore, 1.5sec was selected as $T_{sat,2}$. At T_{sat} = 4sec, the MTR_{asym} curves almost reach a maximum for L-arginine and therefore 4sec was chosen as $T_{sat,1}$. For L-arginine (10mM) with B_0 shifts 0.4 ppm, 0.16 ppm, 0 ppm, and −0.16 ppm, the curves maintain the feature of $MTR_{asym}(T_{sat,1}) > MTR_{asym}(T_{sat,2})$ (Fig.3d). If the LOVARS oscillation patterns are plotted and fit to Eq.[6] (Fig.3e), the phase varies <5%, (Fig. 3f), while the uncorrected MTR_{asym} (Imaginary component) varies 30% (+ 0.16 ppm) or 41.7% (−0.16 ppm).

LOVARS phase map—Fig.4a shows the distribution of samples in the phantom designed to test the capabilities of LOVARS, including four concentrations of L-arginine, three concentrations of agar, two concentrations of crosslinked BSA, and PBS. Fig.4b displays the WASSR B_0 map, with the B_0 shift varying from 0 to 0.5 ppm. Fig.4c and d display the MTR_{asym} maps at ±1.8 ppm for t_{sat} = 1.5sec and 4sec, respectively. L-arginine tubes are highlighted through CEST contrast (PTR) that increases from t_{sat} = 1.5sec to 4sec. MTC tubes also display contrast when their B_0 shift > 0.2 ppm, however this contrast (MTR_{asym}^{field}) is either the same or smaller as t_{sat} increases. The OIC MTR_{asym} map is displayed in Fig.4e, with the high-concentration L-arginine tubes highlighted. It is difficult to detect tubes containing lower concentrations of L-arginine or to discriminate these from agar or BSA. Figs.4i&k display how the pattern of water signal can be manipulated with the LOVARS scheme for tubes containing L-arginine and agar when 2 LUs are collected. The signal patterns can be Fourier-transformed or fit to Eq.[6] (GLM), with the FFT results shown in Figs. 4j and l. After FFT, the magnitude of the real and imaginary components at 1 cycle/LU is nearly the same in the agar tubes (Fig.4l), whereas the imaginary component dominates in L-arginine tubes (Fig.4j) indicating that the LOVARS phase (φ in Eq.[6]) can be used to detect the presence of CEST contrast (PTR). Here we constrained the phase range to $-\pi < \varphi < \pi$ The experimental LOVARS phase map is shown in Fig.4f. The phase for all but one of the BSA, agar and PBS tubes $\leq 3\pi/10$, even with a B_0 inhomogeneity offset of up to 0.5 ppm, while the phase for the L-arginine tubes is $>3\pi/10$. For one PBS tube (3rd row, 2nd column), the phase varies widely due to MTR_{asym} almost equaling 0 and the noise dominates. To avoid this, the phase range of $[3\pi/4, \pi]$ was unwrapped to $[-5\pi/4, -\pi]$. Fig. 4g shows only CEST tubes possess a phase within $\pi/2 > \varphi > 3\pi/10$, eliminating all the MTC and PBS tubes regardless of the B_0 inhomogeneity. In addition, the LOVARS contrast maps (Fig.4f–h) appear less noisy than the OIC-based MTR_{asym} map (Fig.4e). For quantitative

comparison, Table 1 shows the number of scans, the total scan time, and the CNR for both LOVARS and OIC methods. The "CNR efficiency", which equals the CNR divided by square root of the scan time (59), is used to evaluate the performance of the 2 methods. From the table we can see that LOVARS phase has about 2 times the CNR efficiency of the OIC method.

Tolerance to B_0-shift and noise—We further performed a series of simulations to test the limits of LOVARS phase mapping scheme in the presence of B_0 shifts and noise (Fig.5). Two different CEST agents were used: L-arginine and PLL, which possess exchangeable protons at 1.8 ppm and 3.6ppm separated from water, and compared with the phase value produced by the MTC agent agar. Fig.5a displays how the phase changes for three different concentrations of L-arginine and agar. The phase varies slightly with concentration and B_0 shift for L-arginine, and provided the B_0 shift is between −0.2 to +1.2 ppm, this phase can be used to discriminate L-arginine from agar using the criterium $\pi/2>\varphi>3\pi/10$. For shifts ranging from −0.2 to −1.2 ppm, L-arginine can be discriminated using the criterion $\varphi>5\pi/4$. Next, we determined how this scheme would perform for PLL, which has exchangeable protons twice the resonance frequency of L-arginine (Figs.1a&b) with the center at 3.6 ppm. Fig.5b shows how the LOVARS phase varies for PLL and agar using the LOVARS scheme when the saturation pulse is set at 3.6 ppm, where the LOVARS phase criterium $\pi/2>\varphi>\pi/4$ can be used to discriminate PLL from agar for a wide range of B_0 shifts (−0.8 to +1ppm). Figs.5c&d display how the phase depends on the water relaxation times, with the variation shown covering most brain tissues at field strengths of 4.7T, 9.4T and 11.7T (60). The criteria of LOVARS phase mapping are shown schematically in Fig.5e, owing to the feature of $PTR(T_{sat,1})>PTR(T_{sat,2})>0$ for phantoms and extending to $PTR(T_{sat,1})>PTR(T_{sat,2})$ for *in vivo* imaging. We also investigated how the phase changes as a function of concentration and exchange rate through titrating three different concentrations of PLL (10 mg/ml, 5 mg/ml and 2.5 mg/ml) from pH 6.4 to 7.9 (Fig.5f). To determine how LOVARS performs as the SNR of the images change, simulations were performed at 11.7T using 2.5 mM L-arginine and 2% agar (Fig.6). Reduced SNR introduced an uncertainty in the measurement of the phase, however even with 3% noise (Fig.6c) there is a clear separation between L-arginine and agar for B_0 shifts varying up to 1.2 ppm, with a trend very similar for PBS. The phase for agar has a maximum of $\sim 3\pi/10$.

In Vivo Imaging—To test the performance of the scheme *in vivo*, we acquired LOVARS images on mice bearing 9L gliosarcomas, which are expected to show amide proton transfer contrast at an offset of 3.5 ppm. Similar to the phantom experiments, $T_{sat,1}$ and $T_{sat,2}$ were chosen based on examination of the t_{sat}-dependence of MTR_{asym} in tumor and contralateral control tissue. The average MTR_{asym} in tumors plateaued at a t_{sat} = 3 sec which we used for $T_{sat,1}$. $T_{sat,2}$ was set to 0.8sec to satisfy $MTR_{asym}(T_{sat,2}) \sim 0.5 * MTR_{asym}(T_{sat,1})$. Fig.7 displays images of a mouse 8 days after tumor inoculation. The WASSR map (Fig.7b) shows a typical range in B_0 shift from −0.4 ppm to 0.2 ppm across voxels in the brain slice, which distorts the MTR_{asym} map (Fig.7c) generated using only two images with $\Delta\omega$= +3.5 ppm and −3.5 ppm. The artifacts are especially prominent in the lower right hemisphere where there is normal brain tissue but water is shifted +0.2 ppm. However, when 2 LUs are acquired (8 scans) and the signal is followed for ROIs enclosing either the tumor (ROI1) or poorly shimmed control brain tissue (ROI2), as was the case for the phantoms, the LOVARS phases show a large difference between the two ROIs (Fig.7d) despite the fact that the MTR_{asym} (magnitude) is very similar in the uncorrected CEST map (Fig.7c). The LOVARS phase images produced using either FFT or GLM are shown in Figs.7e and f respectively. Alternatively, we can exclude the pixels with $\pi/4>\varphi>-3\pi/4$ to threshold the imaginary component map (uncorrected $MTR_{asym}(T_{sat,1})$ map as in Fig.7c), displays the same

information as the MTR_{asym} map obtained by OIC, but with all 8 images contributing to the CNR of the contrast map.

Next, we examined the variation in the LOVARS phase maps from day 5 to day 11 after cell engraftment. Tumors could clearly be detected in these LOVARS phase (Figs.8a–d: top) and filtered imaginary maps (Figs.8a–d: middle), which compared favorably to those collected using OIC (Fig.8a,b: bottom) and after administration of Gd-DTPA (Fig.8c: bottom), as validated with H&E staining (Fig.8d : bottom). As shown in Table2, LOVARS phase provides dramatic contrast for tumors (average $\varphi = 1.12$ radians or $\sim\pi/3$) over normal brain tissue (average $\varphi = -2.47$ radians or $\sim -4\pi/5$), with a p-value of less than 0.001. The LOVARS contrast maps possess a higher CNR than the OIC maps, with the average CNR for the phase maps ~26.7 (2 LUs) vs. ~8.8 for OIC over the total 11 images on 7 mice and multiple days (Table 2). Table 2 also lists the scan times for LOVARS and the two OIC methods, showing that LOVARS achieves ~ 3.2 times CNR efficiency of that for OIC Scheme 2.

DISCUSSION

A new imaging scheme was constructed with the purposes of allowing the use of time domain analysis techniques to correct for B_0 inhomogeneity and achieve a higher CNR. Another time domain analysis technique for CEST has been proposed recently (61). The LOVARS scheme (Fig.2) takes advantage of the simulations we performed previously using t_{sat} to quantify exchange rates (56), and the large difference in symmetry with respect to the water proton frequency between CEST and MTC, DS. Alternative patterns can be chosen which produce more oscillations of MTC and DS per LU. However we decided to use this 4-point pattern based on its simplicity and efficiency (4 images produce 1 oscillation of CEST contrast and 2 oscillations of MTC and DS). We chose to test this sequence first using L-arginine, because at 1.8 ppm (L-arginine's main chemical shift) there is a significant amount of DS (~15%), which is similar to *in-vivo* brain tumor studies (Figs.1b and 3a) where both MTC and CEST are present within one voxel.

For determining appropriate t_{sat} values for the LOVARS scheme, we used both simulations and experimental phantom data on multiple concentrations of L-arginine and agar (Figs.3b–d). In order to cosine modulate the water signal, we chose $T_{sat,1} = 4$ sec and $T_{sat,2} = 1.5$ sec which allowed us to produce the patterns in Figs.4i&k. As mentioned above, several LOVARS maps can be created using this imaging scheme: a real component map, an imaginary component map and a phase map. The phase map was found to be the least sensitive to B_0 inhomogeneity, and can be used to differentiate CEST from MT and DS. B_0 variation distorts the magnitude of the oscillations in LOVARS (Fig.3e) but produces very slight changes in the phase (Fig.3f). For voxels with only MT and/or DS, the phase remains nearly the same as B_0 varies from −1.6 ppm to 1.6 ppm for Agar (Fig.5a&b). For voxels possessing CEST contrast the phase remains within the CEST phase range, provided the offset of the saturation pulse is such that the pulse at least partially saturates the exchangeable protons. As such, the width at half height of the CEST contrast peak determines the tolerance to B_0 shifts. For our phantom using $B_1 = 3.8$ μT, the width was ~0.8 ppm (Fig.3a). Provided the B_0 variation over the image is less than this, the images produced were very clean (Fig.4g).

Another benefit of the LOVARS method is that it significantly reduces the Specific Absorption Rate (SAR) compared to OIC by decreasing the duty cycle. For our phantom experiments, the duty cycle for 1 LU (4 scans) is 45% less than for OIC, and for *in vivo* the duty cycle of LOVARS is 58% less than the OIC duty cycle.

One feature of the LOVARS phase map is that the phase is insensitive to concentration and exchange rate, as is shown for the 4 different L-arginine concentrations in Fig.4 and for the PLL data in Fig.5f. Here fourfold changes in concentration and sixteenfold changes in the exchange rate result in relative small changes in the LOVARS phase (φ) which are very small (<10%). For the same samples, the MTR_{asym} varies from 4% to 40% as shown in Fig. S2 (>90% change). This is because of the relationship of phase to PTR, with $\tan(\varphi) = MTR_{asym}(T_{sat,1})/MTR_{asym}(T_{sat,2})$ which results in removal of the prefactor $\frac{k_{sw}\cdot\alpha\cdot X_s}{R_{1w}+k_{sw}\cdot X_s}$ (in Eq.[3]). This leads to the phase being less sensitive to the exchange rate (k_{sw}), concentration (X_s) and water relaxation times, although the absolute value of the phase may still exhibit small changes in particular with water T_2 (Figs. 5c, d, f). In addition, the projection from $\tan(\varphi)$ to φ also diminishes the sensitivity. If this insensitivity is undesirable, the LOVARS phase filtered imaginary map can be displayed and this is sensitive to concentration and exchange rate.

Based on the robustness of this scheme *in vitro*, we moved on to testing this in mice. We chose to test this for APT imaging of 9L brain tumors as the APT contrast is well characterized (52), (~5% CEST contrast between tumor and normal tissue) and also because APT imaging of brain tumors is the first clinical application of CEST imaging, having been applied to more than 12 patients (14). We optimized this scheme on 3 mice, with several representative images shown (Figs.7 and 8). The LOVARS phase is significantly different between tumor and control tissue (Table2), and the phase map is less sensitive to B_0 than the standard MTR_{asym} map (Figs.7c,e,f). The LOVARS phase threshold had to be modified to exclude pixels with $-3\pi/4<\varphi<\pi/4$, because normal white and gray matter produced a negative MTR_{asym} at the power levels used and thus in tumors the total MTR_{asym} is either less negative or slightly positive. Based on all the images we have obtained, the B_0 correction range within LOVARS images was ~±0.35 ppm *in vivo*, above which normal brain tissue started to show contrast, compared to the ~0.8 ppm for the phantom. As a result, LOVARS is well suited for brain imaging as B_0 shifts are expected to not exceed this range for mouse brains at this field and for human brains at fields of 7T or lower. The LOVARS phase maps compared favorably to both the conventional APT image obtained using OIC and the Gd-enhanced image. We have not found meaningful differences between the FFT or GLM methods (Figs.7e&f) although this might change for other applications. In addition, the maps produced by this scheme possess a much higher CNR (Fig.8, Table 1) than conventional MTR_{asym} maps due to the acquisition of more LUs and the time domain post-processing, allowing each pair of images to contribute to the total CNR of the maps. We are currently investigating alternative LOVARS schemes to reduce scanning time, B_0 sensitivity, and improve the quantitative capabilities (61).

CONCLUSION

We have developed a new scheme for collecting CEST images based on saturation length and offset variations (LOVARS). Based on our results, the LOVARS phase maps showed some useful properties: 1) CEST contrast regions can be more readily identified in LOVARS phase maps as compared to conventional OIC MTR_{asym} maps while collecting either the same or a smaller number of images. 2) they are less sensitive to B_0 inhomogeneity than conventional approaches; and 3) every pair of images acquired contributes to the CNR of the LOVARS phase maps. When testing this method for detection of 9L gliosarcomas, the resulting images allowed a clear separation of tumor and normal tissue with a CNR four times better than conventional imaging under equivalent acquisition times. The LOVARS scheme appears well suited for use in a wide variety of *in vivo* CEST imaging applications.

Supplementary Material

Refer to Web version on PubMed Central for supplementary material.

Acknowledgments

We are grateful to Dr. Yoshinori Kato for help with the Gd-DTPA injections, Chulani Galpoththawela (B.S.) for help with cell and tissue culture, and Dr. Jiangyang Zhang for help with data acquisition. The project was supported by the Pearl and Yueh-Heng Yang Foundation and NIH grants R21 EB005252, R21 EB008769, R21 NS065284, R01 EB012590, R01 EB015031, and R01 EB015032.

REFERENCES

1. Ward KM, Aletras AH, Balaban RS. A new class of contrast agents for MRI based on proton chemical exchange dependent saturation transfer (CEST). J Magn Reson. 2000; 143(1):79–87. [PubMed: 10698648]
2. Zhou JY, van Zijl PCM. Chemical exchange saturation transfer imaging and spectroscopy. Progress in Nuclear Magnetic Resonance Spectroscopy. 2006; 48(2–3):109–136.
3. van Zijl PC, Yadav NN. Chemical exchange saturation transfer (CEST): What is in a name and what isn't? Magn Reson Med. 2011; 65(4):927–948. [PubMed: 21337419]
4. Aime S, Delli Castelli D, Terreno E. Highly sensitive MRI chemical exchange saturation transfer agents using liposomes. Angew Chem Int Ed Engl. 2005; 44(34):5513–5515. [PubMed: 16052647]
5. Sherry AD, Woods M. Chemical exchange saturation transfer contrast agents for magnetic resonance imaging. Annu Rev Biomed Eng. 2008; 10:391–411. [PubMed: 18647117]
6. Gilad AA, McMahon MT, Walczak P, Winnard PT Jr, Raman V, van Laarhoven HW, Skoglund CM, Bulte JW, van Zijl PC. Artificial reporter gene providing MRI contrast based on proton exchange. Nat Biotechnol. 2007; 25(2):217–219. [PubMed: 17259977]
7. Sun PZ, Zhou J, Sun W, Huang J, van Zijl PC. Detection of the ischemic penumbra using pH-weighted MRI. J Cereb Blood Flow Metab. 2007; 27(6):1129–1136. [PubMed: 17133226]
8. Zhou J, Tryggestad E, Wen Z, Lal B, Zhou T, Grossman R, Wang S, Yan K, Fu DX, Ford E, Tyler B, Blakeley J, Laterra J, van Zijl PC. Differentiation between glioma and radiation necrosis using molecular magnetic resonance imaging of endogenous proteins and peptides. Nat Med. 17(1):130–134. [PubMed: 21170048]
9. Longo DL, Dastru W, Digilio G, Keupp J, Langereis S, Lanzardo S, Prestigio S, Steinbach O, Terreno E, Uggeri F, Aime S. Iopamidol as a responsive MRI-chemical exchange saturation transfer contrast agent for pH mapping of kidneys: In vivo studies in mice at 7 T. Magn Reson Med. 2010; 65(1):202–211. [PubMed: 20949634]
10. Vasalatiy O, Gerard RD, Zhao P, Sun X, Sherry AD. Labeling of adenovirus particles with PARACEST agents. Bioconjug Chem. 2008; 19(3):598–606. [PubMed: 18254605]
11. Vinogradov E, He H, Lubag A, Balschi JA, Sherry AD, Lenkinski RE. MRI detection of paramagnetic chemical exchange effects in mice kidneys in vivo. Magn Reson Med. 2007; 58(4): 650–655. [PubMed: 17899603]
12. Liu G, Li Y, Pagel MD. Design and characterization of a new irreversible responsive PARACEST MRI contrast agent that detects nitric oxide. Magn Reson Med. 2007; 58(6):1249–1256. [PubMed: 18046705]
13. Ling W, Regatte RR, Navon G, Jerschow A. Assessment of glycosaminoglycan concentration in vivo by chemical exchange-dependent saturation transfer (gagCEST). Proceedings of the National Academy of Sciences of the United States of America. 2008; 105(7):2266–2270. [PubMed: 18268341]
14. Wen Z, Hu S, Huang F, Wang X, Guo L, Quan X, Wang S, Zhou J. MR imaging of high-grade brain tumors using endogenous protein and peptide-based contrast. Neuroimage. 51(2):616–622. [PubMed: 20188197]
15. Zhou J, Payen JF, Wilson DA, Traystman RJ, van Zijl PC. Using the amide proton signals of intracellular proteins and peptides to detect pH effects in MRI. Nat Med. 2003; 9(8):1085–1090. [PubMed: 12872167]

16. Salhotra A, Lal B, Laterra J, Sun PZ, van Zijl PC, Zhou J. Amide proton transfer imaging of 9L gliosarcoma and human glioblastoma xenografts. NMR Biomed. 2008; 21(5):489–497. [PubMed: 17924591]

17. McMahon MT, Gilad AA, DeLiso MA, Berman SM, Bulte JW, van Zijl PC. New "multicolor" polypeptide diamagnetic chemical exchange saturation transfer (DIACEST) contrast agents for MRI. Magn Reson Med. 2008; 60(4):803–812. [PubMed: 18816830]

18. Aime S, Carrera C, Delli Castelli D, Geninatti Crich S, Terreno E. Tunable imaging of cells labeled with MRI-PARACEST agents. Angew Chem Int Ed Engl. 2005; 44(12):1813–1815. [PubMed: 15723362]

19. Meldrum T, Seim KL, Bajaj VS, Palaniappan KK, Wu W, Francis MB, Wemmer DE, Pines A. A xenon-based molecular sensor assembled on an MS2 viral capsid scaffold. J Am Chem Soc. 132(17):5936–5937. [PubMed: 20392049]

20. Ali MM, Woods M, Suh EH, Kovacs Z, Tircso G, Zhao P, Kodibagkar VD, Sherry AD. Albumin-binding PARACEST agents. J Biol Inorg Chem. 2007; 12(6):855–865. [PubMed: 17534672]

21. Zhao JM, Har-el YE, McMahon MT, Zhou J, Sherry AD, Sgouros G, Bulte JW, van Zijl PC. Size-induced enhancement of chemical exchange saturation transfer (CEST) contrast in liposomes. J Am Chem Soc. 2008; 130(15):5178–5184. [PubMed: 18361490]

22. Winter PM, Cai K, Chen J, Adair CR, Kiefer GE, Athey PS, Gaffney PJ, Buff CE, Robertson JD, Caruthers SD, Wickline SA, Lanza GM. Targeted PARACEST nanoparticle contrast agent for the detection of fibrin. Magn Reson Med. 2006; 56(6):1384–1388. [PubMed: 17089356]

23. Langereis S, Keupp J, van Velthoven JL, de Roos IH, Burdinski D, Pikkemaat JA, Grull H. A temperature-sensitive liposomal 1H CEST and 19F contrast agent for MR image-guided drug delivery. J Am Chem Soc. 2009; 131(4):1380–1381. [PubMed: 19173663]

24. Li AX, Wojciechowski F, Suchy M, Jones CK, Hudson RH, Menon RS, Bartha R. A sensitive PARACEST contrast agent for temperature MRI: Eu3+-DOTAM-glycine (Gly)-phenylalanine (Phe). Magn Reson Med. 2008; 59(2):374–381. [PubMed: 18228602]

25. Wu Y, Soesbe TC, Kiefer GE, Zhao P, Sherry AD. A responsive europium(III) chelate that provides a direct readout of pH by MRI. J Am Chem Soc. 132(40):14002–14003. [PubMed: 20853833]

26. Kalman FK, Baranyai Z, Toth I, Banyai I, Kiraly R, Brucher E, Aime S, Sun X, Sherry AD, Kovacs Z. Synthesis, potentiometric, kinetic, and NMR Studies of 1,4,7,10-tetraazacyclododecane-1,7-bis(acetic acid)-4,10-bis(methylenephosphonic acid) (DO2A2P) and its complexes with Ca(II), Cu(II), Zn(II) and lanthanide(III) ions. Inorg Chem. 2008; 47(9):3851–3862. [PubMed: 18380456]

27. Zhang S, Trokowski R, Sherry AD. A paramagnetic CEST agent for imaging glucose by MRI. J Am Chem Soc. 2003; 125(50):15288–15289. [PubMed: 14664562]

28. Huang CH, Morrow JR. A PARACEST agent responsive to inner- and outer-sphere phosphate ester interactions for MRI applications. J Am Chem Soc. 2009; 131(12):4206–4207. [PubMed: 19317496]

29. Henkelman RM, Huang X, Xiang QS, Stanisz GJ, Swanson SD, Bronskill MJ. Quantitative interpretation of magnetization transfer. Magn Reson Med. 1993; 29(6):759–766. [PubMed: 8350718]

30. Eng J, Ceckler TL, Balaban RS. Quantitative 1H magnetization transfer imaging in vivo. Magn Reson Med. 1991; 17(2):304–314. [PubMed: 2062205]

31. Baguet E, Roby C. Off-resonance irradiation effect in steady-state NMR saturation transfer. J Magn Reson. 1997; 128(2):149–160. [PubMed: 9356270]

32. Grad J, Mendelson D, Hyder F, Bryant RG. Direct Measurements of Longitudinal Relaxation and Magnetization Transfer in Heterogeneous Systems. Journal of Magnetic Resonance. 1990; 86(2): 416–419.

33. Zhou J, Wilson DA, Sun PZ, Klaus JA, Van Zijl PC. Quantitative description of proton exchange processes between water and endogenous and exogenous agents for WEX, CEST, and APT experiments. Magn Reson Med. 2004; 51(5):945–952. [PubMed: 15122676]

34. Pekar J, Jezzard P, Roberts DA, Leigh JS Jr, Frank JA, McLaughlin AC. Perfusion imaging with compensation for asymmetric magnetization transfer effects. Magn Reson Med. 1996; 35(1):70–79. [PubMed: 8771024]
35. Hua J, Jones CK, Blakeley J, Smith SA, van Zijl PC, Zhou J. Quantitative description of the asymmetry in magnetization transfer effects around the water resonance in the human brain. Magn Reson Med. 2007; 58(4):786–793. [PubMed: 17899597]
36. Zhou J, Blakeley JO, Hua J, Kim M, Laterra J, Pomper MG, van Zijl PC. Practical data acquisition method for human brain tumor amide proton transfer (APT) imaging. Magn Reson Med. 2008; 60(4):842–849. [PubMed: 18816868]
37. Stancanello J, Terreno E, Castelli DD, Cabella C, Uggeri F, Aime S. Development and validation of a smoothing-splines-based correction method for improving the analysis of CEST-MR images. Contrast Media Mol Imaging. 2008; 3(4):136–149. [PubMed: 18683280]
38. Sun PZ, Farrar CT, Sorensen AG. Correction for artifacts induced by B(0) and B(1) field inhomogeneities in pH-sensitive chemical exchange saturation transfer (CEST) imaging. Magn Reson Med. 2007; 58(6):1207–1215. [PubMed: 17969015]
39. Kim M, Gillen J, Landman BA, Zhou J, van Zijl PC. Water saturation shift referencing (WASSR) for chemical exchange saturation transfer (CEST) experiments. Magn Reson Med. 2009; 61(6): 1441–1450. [PubMed: 19358232]
40. Liu G, Gilad AA, Bulte JW, van Zijl PC, McMahon MT. High-throughput screening of chemical exchange saturation transfer MR contrast agents. Contrast Media Mol Imaging. 2010; 5(3):162–170. [PubMed: 20586030]
41. Terreno E, Stancanello J, Longo D, Castelli DD, Milone L, Sanders HM, Kok MB, Uggeri F, Aime S. Methods for an improved detection of the MRI-CEST effect. Contrast Media Mol Imaging. 2009; 4(5):237–247. [PubMed: 19839029]
42. Shah T, Lu L, Dell KM, Pagel MD, Griswold MA, Flask CA. CEST-FISP: a novel technique for rapid chemical exchange saturation transfer MRI at 7 T. Magn Reson Med. 65(2):432–437. [PubMed: 20939092]
43. Li Y, Sheth VR, Liu G, Pagel MD. A self-calibrating PARACEST MRI contrast agent that detects esterase enzyme activity. Contrast Media Mol Imaging.
44. Scheidegger R, Vinogradov E, Alsop DC. Amide proton transfer imaging with improved robustness to magnetic field inhomogeneity and magnetization transfer asymmetry using saturation with frequency alternating RF irradiation. Magn Reson Med. 2011
45. Bandettini PA, Jesmanowicz A, Wong EC, Hyde JS. Processing Strategies for Time-Course Data Sets in Functional Mri of the Human Brain. Magnet Reson Med. 1993; 30(2):161–173.
46. Cox RW. AFNI: software for analysis and visualization of functional magnetic resonance neuroimages. Comput Biomed Res. 1996; 29(3):162–173. [PubMed: 8812068]
47. McKeown MJ, Makeig S, Brown GG, Jung TP, Kindermann SS, Bell AJ, Sejnowski TJ. Analysis of fMRI data by blind separation into independent spatial components. Human Brain Mapping. 1998; 6(3):160–188. [PubMed: 9673671]
48. Cohen MS. Parametric analysis of fMRI data using linear systems methods. Neuroimage. 1997; 6(2):93–103. [PubMed: 9299383]
49. Friston KJ, Holmes AP, Worsley KJ, Poline JP, Frith CD, Frackowiak RSJ. Statistical parametric maps in functional imaging: A general linear approach. Human Brain Mapping. 1994; 2(4):189–210.
50. Calhoun VD, Adali T, Pearlson GD, Pekar JJ. Spatial and temporal independent component analysis of functional MRI data containing a pair of task-related waveforms. Human Brain Mapping. 2001; 13(1):43–53. [PubMed: 11284046]
51. Smith SM, Jenkinson M, Woolrich MW, Beckmann CF, Behrens TEJ, Johansen-Berg H, Bannister PR, De Luca M, Drobnjak I, Flitney DE, Niazy RK, Saunders J, Vickers J, Zhang YY, De Stefano N, Brady JM, Matthews PM. Advances in functional and structural MR image analysis and implementation as FSL. Neuroimage. 2004; 23:S208–S219. [PubMed: 15501092]
52. Zhou J, Lal B, Wilson DA, Laterra J, van Zijl PC. Amide proton transfer (APT) contrast for imaging of brain tumors. Magn Reson Med. 2003; 50(6):1120–1126. [PubMed: 14648559]

53. Portnoy S, Stanisz GJ. Modeling pulsed magnetization transfer. Magn Reson Med. 2007; 58(1): 144–155. [PubMed: 17659607]
54. Mulkern RV, Williams ML. The general solution to the Bloch equation with constant rf and relaxation terms: application to saturation and slice selection. Med Phys. 1993; 20(1):5–13. [PubMed: 8455512]
55. Woessner DE, Zhang SR, Merritt ME, Sherry AD. Numerical solution of the Bloch equations provides insights into the optimum design of PARACEST agents for MRI. Magnet Reson Med. 2005; 53(4):790–799.
56. McMahon MT, Gilad AA, Zhou J, Sun PZ, Bulte JW, van Zijl PC. Quantifying exchange rates in chemical exchange saturation transfer agents using the saturation time and saturation power dependencies of the magnetization transfer effect on the magnetic resonance imaging signal (QUEST and QUESP): Ph calibration for poly-L-lysine and a starburst dendrimer. Magn Reson Med. 2006; 55(4):836–847. [PubMed: 16506187]
57. Smith SA, Bulte JW, van Zijl PC. Direct saturation MRI: theory and application to imaging brain iron. Magn Reson Med. 2009; 62(2):384–393. [PubMed: 19526497]
58. Li JG, Graham SJ, Henkelman RM. A flexible magnetization transfer line shape derived from tissue experimental data. Magn Reson Med. 1997; 37(6):866–871. [PubMed: 9178237]
59. Liu G, Ali MM, Yoo B, Griswold MA, Tkach JA, Pagel MD. PARACEST MRI with improved temporal resolution. Magn Reson Med. 2009; 61(2):399–408. [PubMed: 19165903]
60. de Graaf RA, Brown PB, McIntyre S, Nixon TW, Behar KL, Rothman DL. High magnetic field water and metabolite proton T1 and T2 relaxation in rat brain in vivo. Magn Reson Med. 2006; 56(2):386–394. [PubMed: 16767752]
61. Friedman JI, McMahon MT, Stivers JT, Van Zijl PC. Indirect detection of labile solute proton spectra via the water signal using frequency-labeled exchange (FLEX) transfer. J Am Chem Soc. 132(6):1813–1815. [PubMed: 20095603]
62. Song X, Chan KW, Liu G, Arifin DA, Gilad AA, Van Zijl PC, Bulte JW, McMahon MT. Imaging of DIACEST Microcapsules Containing Hepatocytes Using Length Variation of Saturation and Principal Component Analysis. Proc Int Soc Magn Reson Med. 2010; 19:1701.

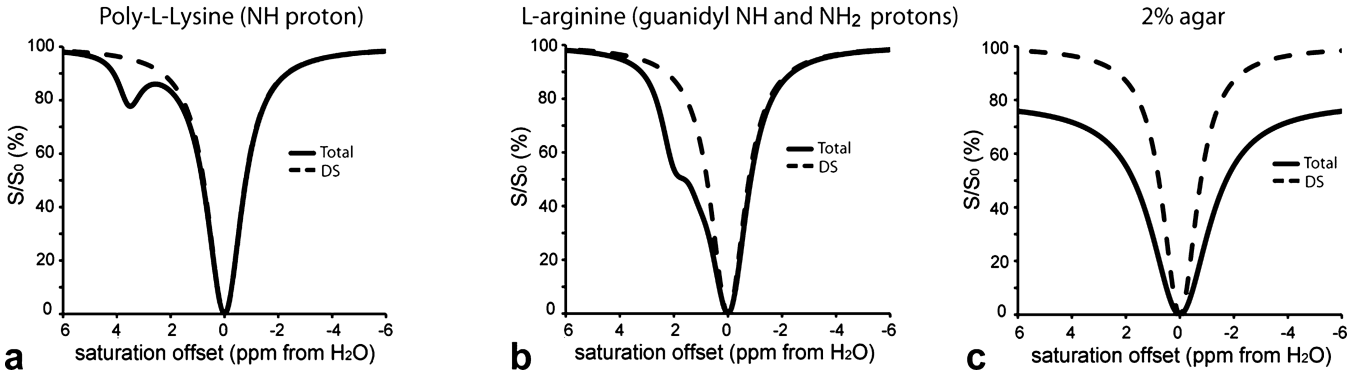

Figure 1.

Simulations of the Z-spectra produced by solutions containing either CEST (PLL or L-arginine) or conventional MTC agents (Agar) to display the symmetries of the various contributions to saturation signal loss. a) Z-spectrum of PLL (solid line) in PBS and second without contrast agent (dash line). b) Z-spectrum for L-arginine (solid line) in PBS and second without contrast agent (dash line). c) Z-spectrum for 2% Agar (solid line) in PBS and second without contrast agent (dash line).

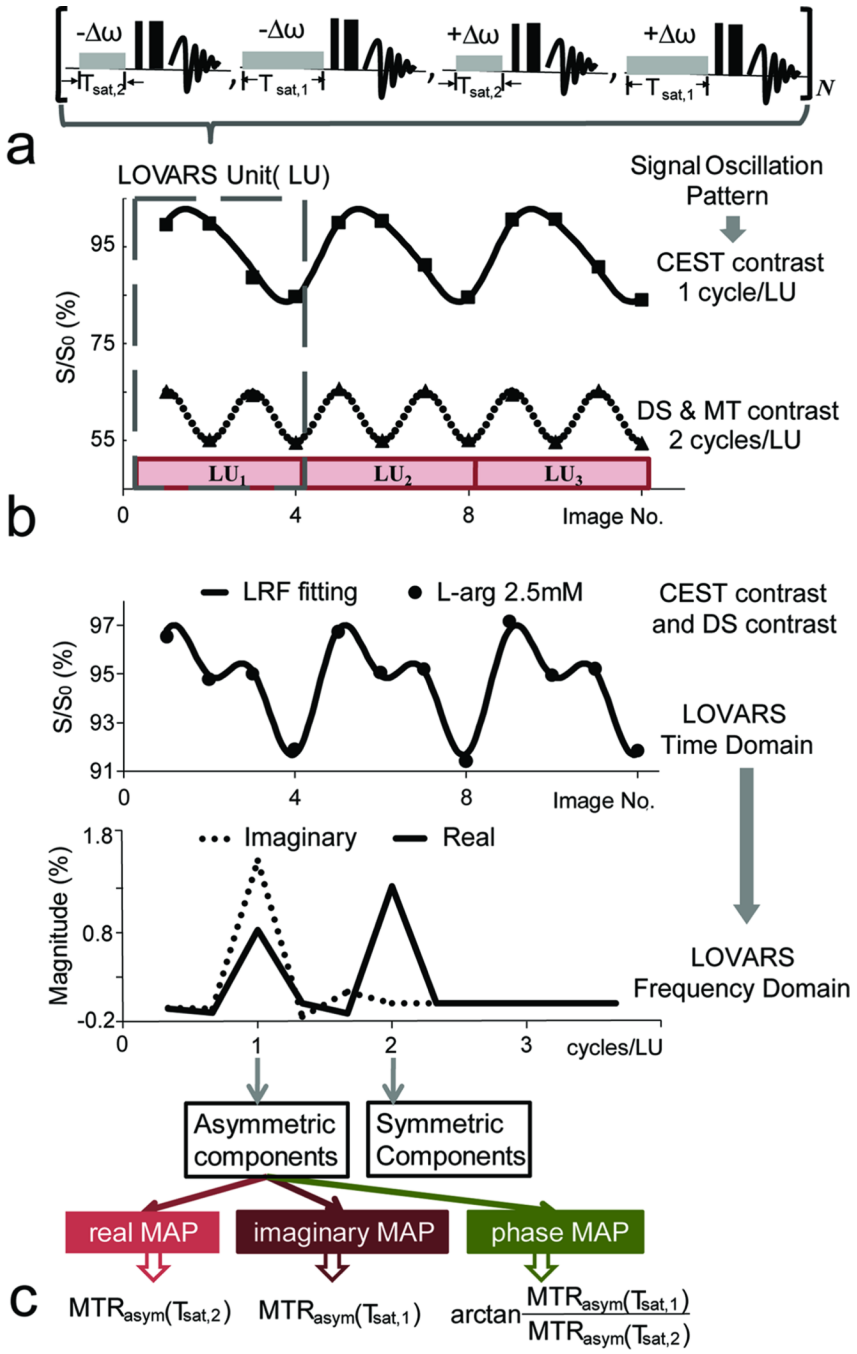

Figure 2.

Illustration of the LOVARS acquisition scheme depicting the oscillation patterns produced in water signal. a) The variation in saturation image LOVARS collection pattern is displayed, with both saturation offset (Δω), and length (t_{sat}) manipulated in a LU, with N total units collected (either 3 or 4 in this study). b) The resulting signal patterns produced on either 5 mg/mL PLL (upper, solid squares) or 4% agar (lower, solid triangles) with the data fit using Eq.[6]. CEST contrast oscillates at 1 cycle/LU and DS and MTC oscillate at 2 cycles/LU. c) The LOVARS signal patterns for L-arginine (2.5mM), Δω = 1.8 ppm, containing both CEST and DS contrast, with the data fit using Eq.[6]. The time domain data

is transformed to the LOVARS frequency domain, generating the new LOVARS parameters for each voxel: real, imaginary and phase values.

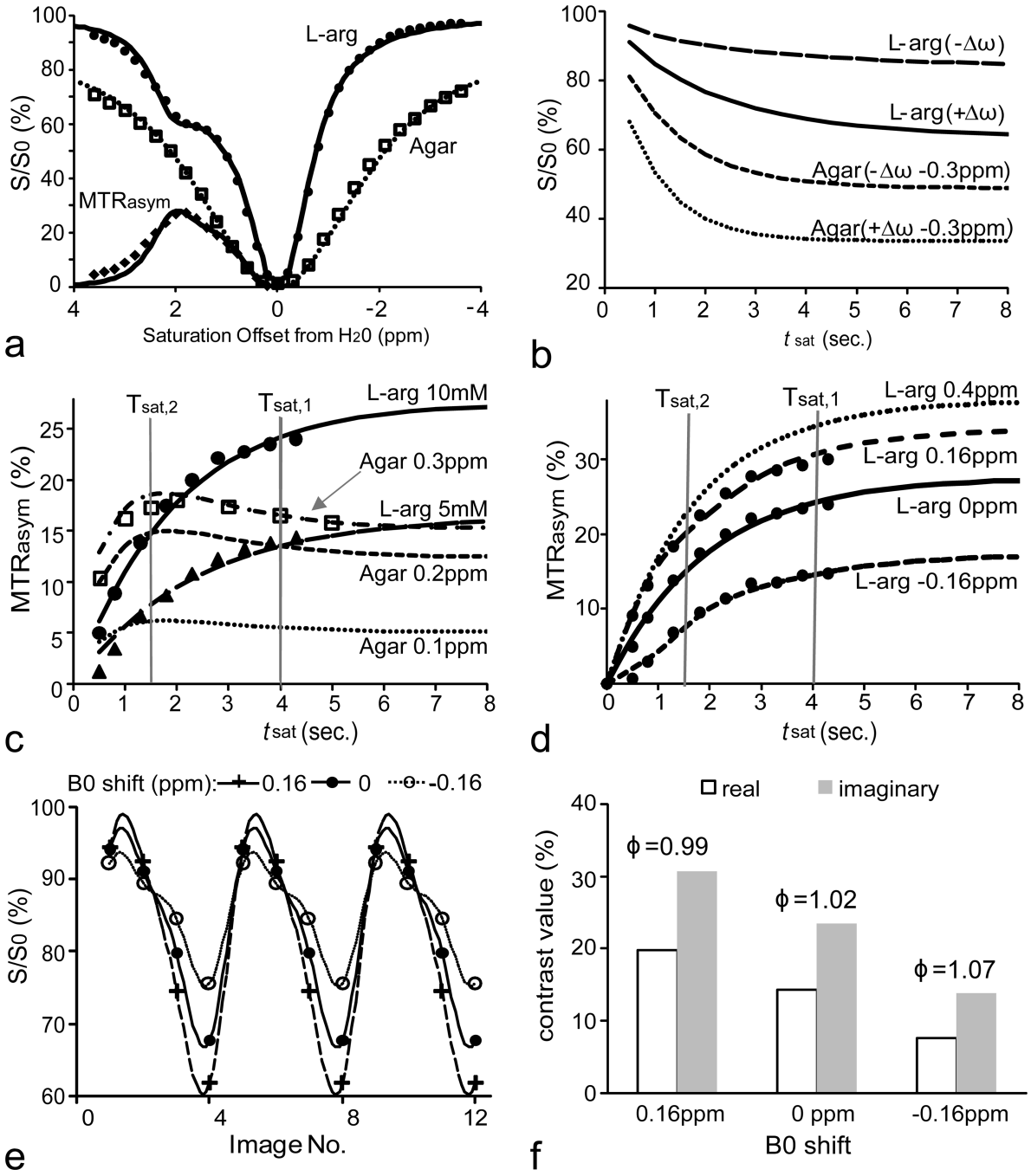

Figure 3.

Comparison between 10 mM L-arginine and 2% agar phantoms at 11.7T using both experiments (symbols) and simulations (lines). a) Experimental Z-spectra (agar and L-arginine) and MTR_{asym} (L-arginine only) curves (symbols) and fitted (line); b) Simulations of water signal changes as function of t_{sat} for saturation offsets of $+\Delta\omega$ or $-\Delta\omega$ for 10mM L-arginine. For 2% agar the signal was plotted with saturation at $+\Delta\omega$ −0.3 ppm and $-\Delta\omega$ −0.3 ppm due to a water frequency shift of 0.3 ppm. c) t_{sat}-dependence of MTR_{asym} for L-arginine (10 mM and 5 mM, saturation at $\pm\Delta\omega$) and for 2% agar with the water frequency shifted by 0.1 ppm, 0.2 ppm and 0.3 ppm. d) MTR_{asym} as a function of t_{sat} for L-arginine (10 mM) with the water frequency shifted by −0.16 ppm, 0 ppm, 0.16 ppm, and 0.4 ppm. e)

LOVARS oscillation patterns and LRF fit for B_0 shifts of −0.16 ppm, 0 ppm and 0.16 ppm. f) FFT transform of patterns in **e**, showing real and imaginary components (and phase on top).

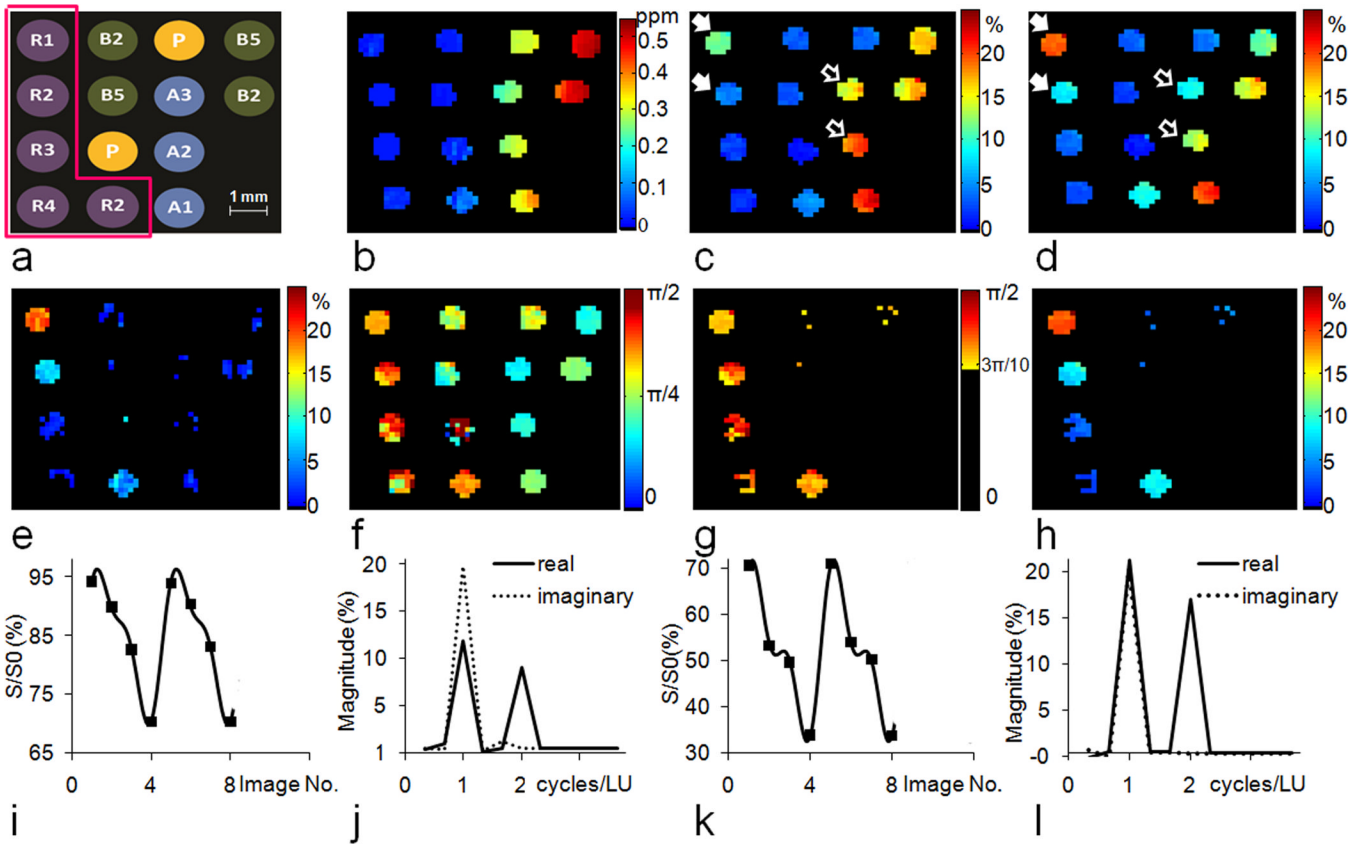

Figure 4.

In vitro test of the performance of the LOVARS phase mapping scheme. a) Configuration of the phantom (**R1–R4:** Arginine 10 mM, 5 mM, 2.5 mM and 1.25 mM at pH = 7.4, **A1–A3:** Agar 2%, 3% and 4%, **B2:** 2.5% heat crosslinked BSA, **B5:** 5% heat crosslinked BSA, **P:** 10 mM PBS; b) is the B_0 shift map obtained using WASSR; c) Uncorrected MTR_{asym} map, $\Delta\omega = \pm 1.8$ ppm, $t_{sat} = 1.5$ sec, which corresponds to a LOVARS real component map; d) Uncorrected MTR_{asym} map, $\Delta\omega = \pm 1.8$ ppm, $t_{sat} = 4$ sec, which corresponds to a LOVARS imaginary component map; The highest concentrations of L-arginine are marked by the solid white arrows, which clearly show that the CEST contrast (PTR) increases from t_{sat} = 1.5 sec to 4 sec. MTC tubes also highlight when the B_0 shift are larger than 100 Hz, however this contrast (MTR_{asym}^{field}) is either the same or smaller as t_{sat} increases from 1.5sec to 4sec. (open white arrows) e) OIC MTR_{asym} map, $\Delta\omega = \pm 1.8$ ppm, $t_{sat} = 4$s; f) LOVARS phase map; g) LOVARS phase map using the thresholds described in Supplementary Material; h) LOVARS imaginary component map using the thresholds described in Supplementary Material; i) Plot of the water signal pattern produced for 8 LOVARS images (2 LUs) in the 10 mM L-arginine tube and j) Real and imaginary components after FFT for 10 mM L-arginine, with imaginary (1 cycle/LU) > real (1 cycle/LU); k) Plot of the water signal pattern produced for 8 LOVARS images (2 LUs) in a 2% agar tube with B_0 shift = 0.3–0.4 ppm and l) the corresponding real and imaginary components after FFT, with imaginary (1 cycle/LU) = real (1 cycle/LU).

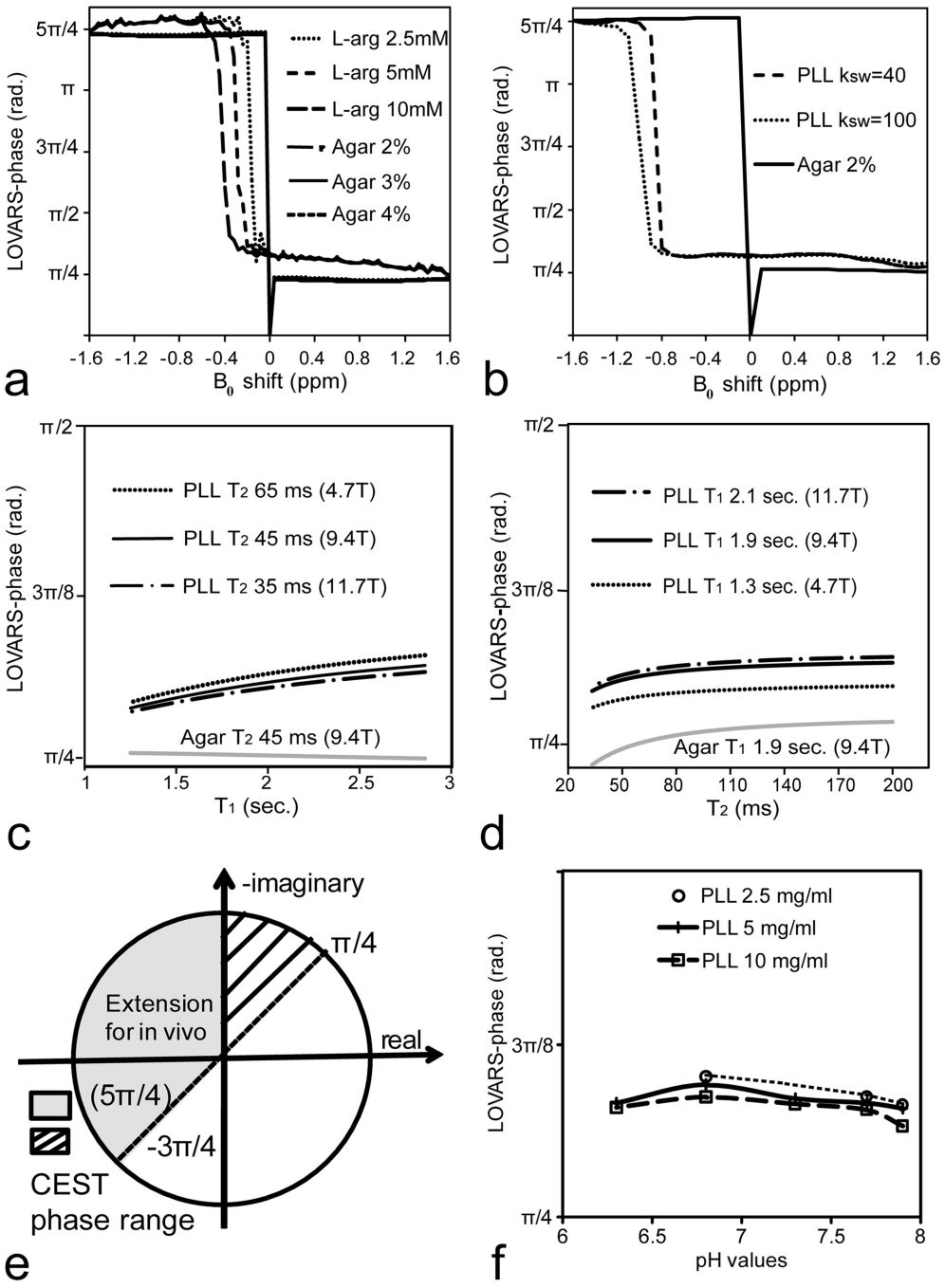

Figure 5.

a) Simulations of LOVARS phase as a function of B0 shift for L-arginine (10 mM, 5 mM, 2.5 mM) and agar (1%, 2%, 4%), $\Delta\omega = \pm 1.8$ ppm, with the resulting phase for all agar samples nearly identical. b) Simulation of LOVARS phase as a function of B0 shift for PLL (k_{sw} = 40, 100) and 2% agar, $\Delta\omega = \pm 3.6$ ppm; c) Simulation of LOVARS phase as a function of water T_1 for PLL (k_{sw} = 40) and 2% Agar, with T_2 set to the average rodent brain value found at 4.7T, 9.4T and 11.7T. d) Simulation of LOVARS phase as a function of T_2 relaxation for PLL (k_{sw}=40) and Agar 2%, with T_1 set to the average rodent brain value found at 4.7T, 9.4T and 11.7T. e) Illustration of phase range restrictions suitable for determining which pixels display CEST contrast; f) LOVARS phase as a function of pH for

three different concentrations of PLL(10mg/ml, 5mg/ml and 2.5mg/ml). The exchange rates varied from ~70 Hz (pH 6.4) to ~1200 Hz (pH 7.9) for these samples.

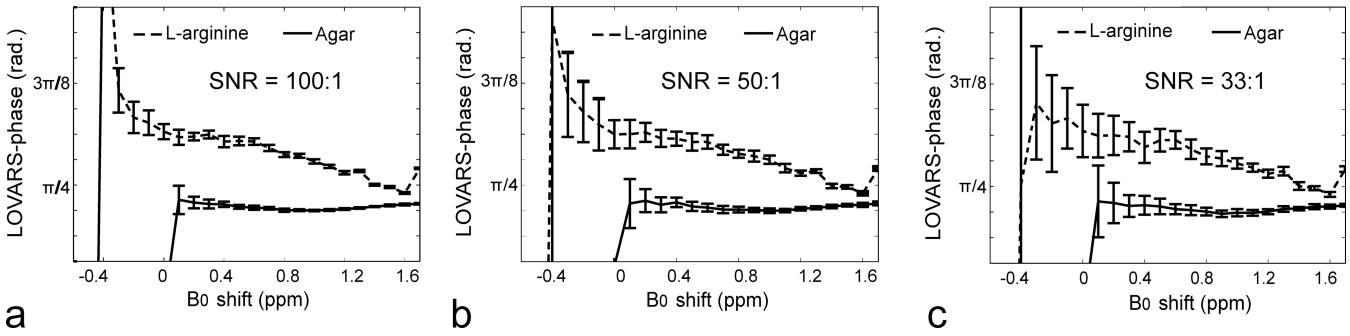

Figure 6.

LOVARS phase as a function of B_0 shift with SNR = 100:1 (a), 50:1 (b) and 33:1 (c) respectively. The error bars indicate the SD values of LOVARS phase based on 20 different synthetic datasets using random noise.

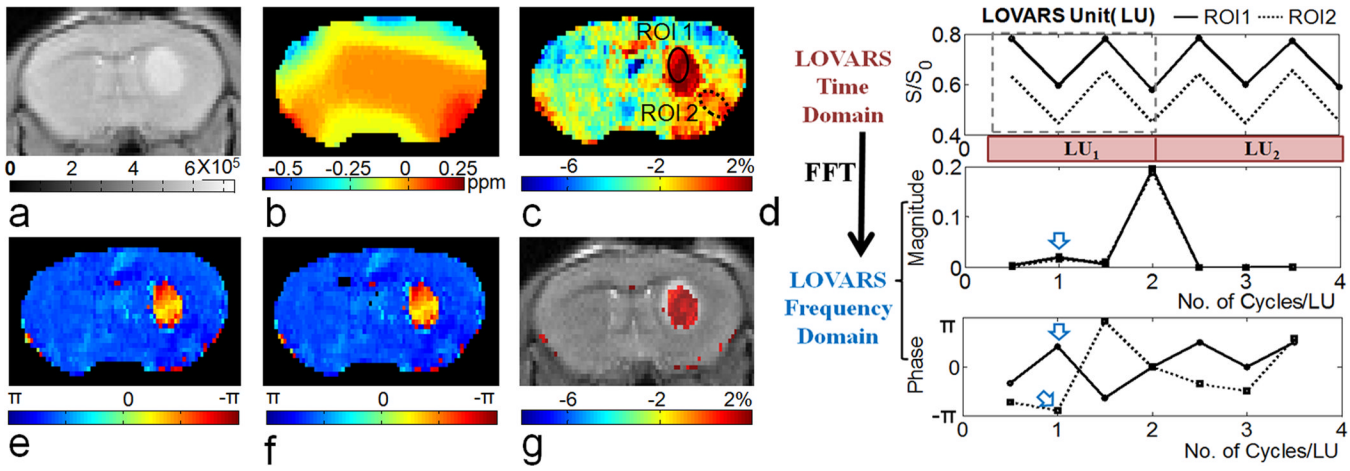

Figure 7.

In vivo demonstration of the LOVARS scheme as applied to the imaging of 9L gliosarcomas in mice. a) T2-w scout image; b) B_0 shift map (WASSR); c) uncorrected MTR_{asym} map; d) LOVARS time domain data (top) with phase (middle) and magnitude (bottom) traces determined through FFT with ROIs as marked in c, ROI1 = tumor region and ROI2 = control tissue with large B_0 shift. The arrows point to the average phase (middle) and magnitude (bottom) in ROI1 and ROI2 at 1cycle/LU based on FFT; e) LOVARS phase map calculated using FFT; f) LOVARS phase map calculated using GLM; g) thresholded LOVARS imaginary component map.

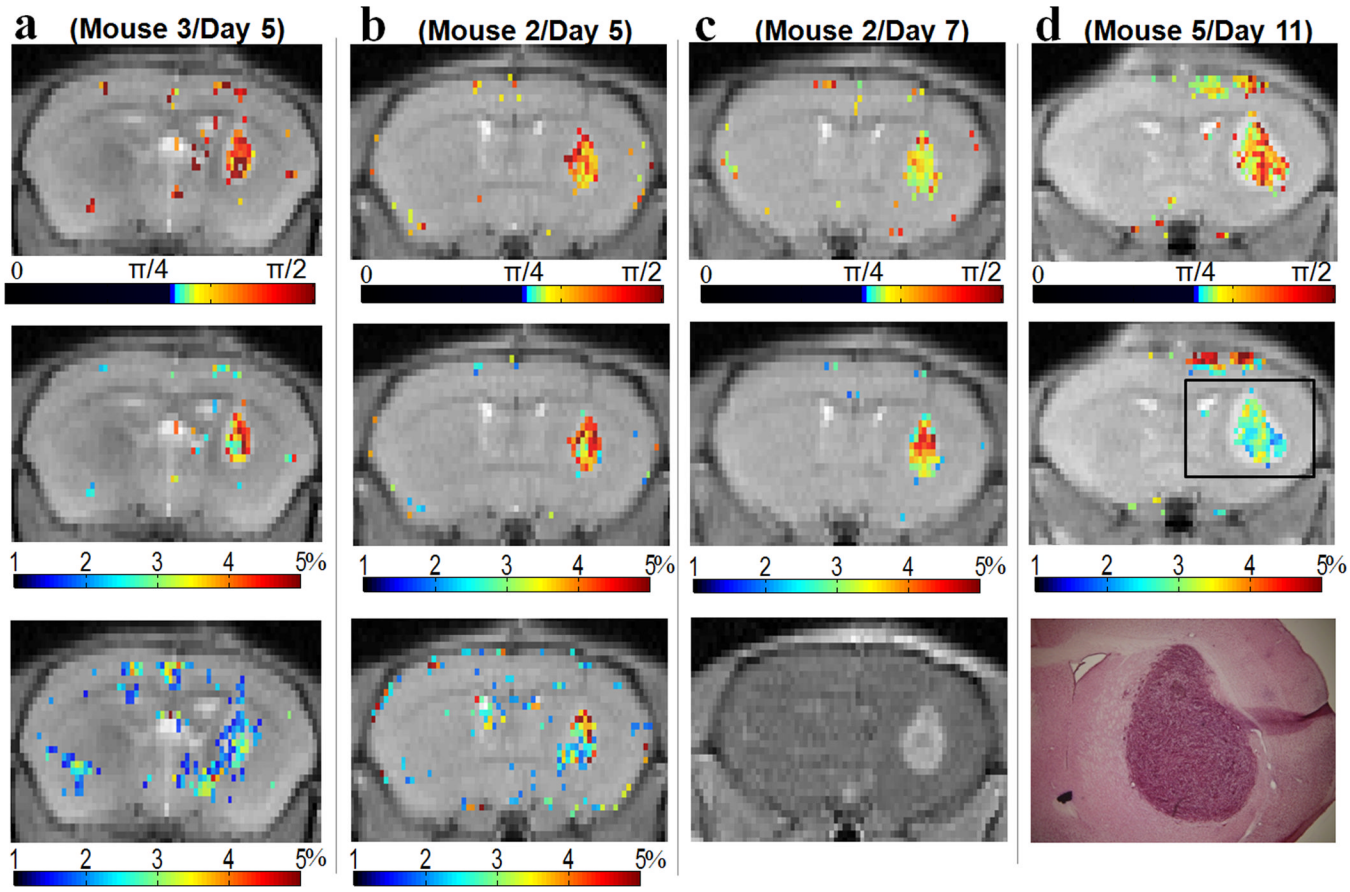

Figure 8.

Four representative LOVARS phase and imaginary component maps acquired 5, 7, and 11 days after tumor engraftment compared with other methods. **a & b**, top: LOVARS phase maps; middle: LOVARS imaginary component maps; bottom: OIC MTR_{asym} map obtained using 6 offsets; **c)&d),** top: LOVARS phase maps; middle: LOVARS imaginary component maps; bottom **c:** T_1-w image collected 30s after administration of Gd-DTPA; bottom **d:** H&E stain after tissue sectioning.

Table 1

Experimental Comparison Between LOVARS and OIC: L-arginine 10mM

	No. of scans	Scan time (sec)	[a]CNR		[b]CNR efficiency ($sec^{-1/2}$)	
			phase	imaginary	phase	imaginary
LOVARS	1 LU (4 scans) + 1 S_0	480	28.5	23.1	1.3	1.1
	2 LUs (8 scans) + 1 S_0	864	38.1	35.7	1.3	1.2
	3 LUs (12 scans) + 1 S_0	1248	56.9	42.9	1.6	1.2
			MTR_{asym}		MTR_{asym}	
OIC	B0 field map(WASSR)	221				
	6 scans + 1 S_0	672	21.4		0.71	
	Total	893				

[a] $CNR_{contrast}$ for a specific contrast is calculated by $\sqrt{2}mean(S_{contrast})/std(S_{contrast,1} - S_{contrast,2})$, where $S_{contrast,1}$ and $S_{contrast,2}$ are the signal intensity of two contrast maps acquired consecutively.

[b] $\text{CNR efficiency}_{contrast} = \text{CNR}_{contrast} / \sqrt{scan\ time}$

Table 2

In vivo comparison of LOVARS and OIC for 9L tumors and control tissue

	LOVARS		OIC	
	Phase (tumor)	Phase (control)	MTR_{asym}(tumor, %)	MTR_{asym}(control, %)
Day5/M2	1.20 ± 0.17	−2.34 ± 0.13	3.6 ± 0.8	−3.0 ± 0.6
Day5/M3	1.30 ± 0.20	−2.61 ± 0.16	2.8 ± 1.0	−3.9 ± 1.0
Day7/M2	1.12 ± 0.14	−2.01 ± 0.14	4.8 ± 0.9	−2.4 ± 0.8
Day8/ M1	1.01 ± 0.17	−2.71 ± 0.11	3.0 ± 0.4	−1.0 ± 0.4
Day8/ M3	1.10 ± 0.29	−2.23 ± 0.09	1.3 ± 0.7	−4.4 ± 0.5
Day10/M7	1.08 ± 0.22	−2.65 ± 0.13	4.8 ± 1.0	−2.0 ± 0.8
Day10/M1	0.97 ± 0.20	−2.65 ± 0.13	2.5 ± 0.7	−2.7 ± 0.6
Day11/M2	1.08 ± 0.13	−2.59 ± 0.14	5.2 ± 0.6	−1.4 ± 0.7
Day11/M4	1.06 ± 0.12	−2.48 ± 0.14	6.4 ± 0.9	−2.7 ± 0.9
Day11/M5	1.20 ± 0.25	−2.23 ± 0.15	2.1 ± 0.8	−4.5 ± 0.9
Day11/M6	1.16 ± 0.14	−2.68 ± 0.16	3.8 ± 0.7	−1.3 ± 0.9
Average value	1.12	−2.47	3.7	−2.7
[a]Average CNR	26.7		8.8	
Scan time (T_{scan})	2 LUs 9 scans X 80 sec/scan		Scheme 1[b] Zspectrum 25 scans X 40sec/scan APT map 7 scans X 80sec/scan	Scheme 2 WASSR 11 scans X 24sec/scan APT map 7 scans X 80sec/scan
	12 min		26 min (total)	13.7 min (total)
[c]CNR efficiency ($sec^{-1/2}$)	1.00		0.22	0.31

[a] $CNR = \sqrt{2}(S^{tumor} - S^{control})/\delta$, where the noise δ is the standard deviation of a 4 pixel by 4 pixel control ROI for the subtraction of 2 consecutively acquired contrast maps;

[b] The optimized offsets for the Z-spectrum were chosen according to Table 2, Reference 14.

[c] CNR efficiency equals to $\mathrm{CNR}_{\mathrm{contrast}} / \sqrt{\mathrm{T}_{\mathrm{scan}}}$;